Simultaneous Etching and Doping of TiO_2 Nanowire Arrays for Enhanced Photoelectrochemical Performance

Yongcheng Wang,[†] Yue-Yu Zhang,[‡] Jing Tang,[†] Haoyu Wu,[†] Ming Xu,[†] Zheng Peng,[†] Xin-Gao Gong,[‡] and Gengfeng Zheng[†,*]

[†]Laboratory of Advanced Materials, Department of Chemistry, Fudan University, Shanghai, 200433, People's Republic of China and [‡]Key Laboratory of Computational Physical Sciences, Ministry of Education, State Key Laboratory of Surface Physics, and Department of Physics, Fudan University, Shanghai, 200433, People's Republic of China

ABSTRACT We developed a postgrowth doping method of TiO_2 nanowire arrays by a simultaneous hydrothermal etching and doping in a weakly alkaline condition. The obtained tungsten-doped TiO_2 core—shell nanowires have an amorphous shell with a rough surface, in which W species are incorporated into the amorphous TiO_2 shell during this simultaneous etching/regrowth step for the optimization of photoelectrochemical performance. Photoanodes made of these W-doped TiO_2 core—shell nanowires show a much enhanced photocurrent density of ~1.53 mA/cm^2 at 0.23 V *vs* Ag/AgCl (1.23 V *vs* reversible hydrogen electrode), almost 225% of that of the pristine TiO_2 nanowire photoanodes. The electrochemical impedance spectroscopy measurement and the density functional theory calculation demonstrate that the substantially improved performance of the dual W-doped and etched TiO_2 nanowires is attributed to the enhancement of charge transfer and the increase of charge carrier density, resulting from the combination effect of etching and W-doping. This unconventional, simultaneous etching and doping of pregrown nanowires is facile and takes place under moderate conditions, and it may be extended for other dopants and host materials with increased photoelectrochemical performances.

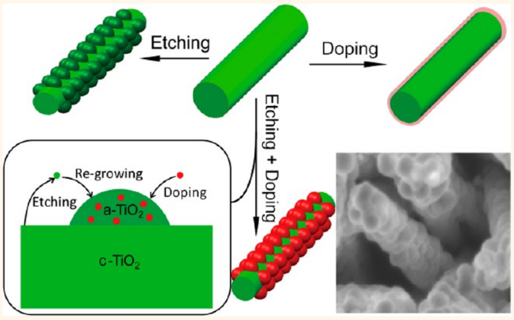

KEYWORDS: photoelectrochemical · TiO_2 · nanowires · doping · etching · density functional theory

The continuing and increasing focus on solar energy-driven photoelectrochemical (PEC) conversion has inspired substantial research development of new semiconducting materials and structures as photoelectrodes,[1−3] among which TiO_2 has remained one of the top research hot spots.[4−7] In particular, one-dimensional (1D) TiO_2 nanostructures such as nanowires (NWs) and nanotubes (NTs), synthesized by hydrothermal growth,[4−6] electrodeposition,[8] electrochemical etching,[9] and sol—gel methods,[10] have been demonstrated as attractive PEC photoanodes, due to their favorable band edge positions *vs* the oxidation/reduction potentials of water, superior 1D charge transport behavior, and excellent chemical stability and photocorrosion resistance.[5,11] However, the PEC performances of these 1D TiO_2 nanostructures are still limited by their wide band gap ($E_g = 3.0-3.2$ eV)[5] and relatively low electron mobility (~0.3 cm^2 V^{-1} s^{-1} for rutile TiO_2).[12] In addition, compared to TiO_2 nanoparticles (NPs)[13] and mesoporous structures,[14] TiO_2 NWs and NTs have lower specific surface areas, thus limiting the electrode/electrolyte interface for the electrochemical reactions. The chemical doping of metal ions, either by monodoping[4] or codoping,[6] has been investigated as a highly promising approach in reducing the TiO_2 band gap and enhancing the charge separation.[2] The incorporation of metal dopants has almost exclusively been achieved during the synthesis step of the TiO_2 nanostructures, such as hydrothermal growth,[4] sol—gel,[13] electrodeposition,[15] and sputtering.[16] Only very limited examples have recently been demonstrated to achieve the postgrowth doping of metal ions, such as the codoping of TiO_2 NWs with tungsten and carbon by a flame annealing process,[6] although the required temperature (~1100 °C) is too high for most of the conducting substrates. Annealing at relatively moderate temperatures (~650—700 °C) is another effective approach for diffusion and activation

* Address correspondence to gfzheng@fudan.edu.cn.

Received for review August 5, 2013 and accepted September 18, 2013.

10.1021/nn4040876

of the existing dopant atoms inside oxides.[17] However, the annealing temperatures required are still too high for many substrates such as fluorine-doped tin oxide (FTO). It is generally challenging for most of the current doping methods to achieve hybrid materials/structures, where the dopants and host materials undergo different growth conditions. Thus, the development of postgrowth doping approaches may allow for modulated doping profiles such as core–shell within individual nanostructures, as the doping steps are sequentially processed with the existing host structures.

On the other hand, the chemical etching/regrowth of TiO_2 represents an unconventional approach for obtaining TiO_2 hierarchical structures. It has been reported that TiO_2 NTs can be formed by hydrothermal treatment of TiO_2 NPs with strong bases,[18,19] and the proposed mechanism is that the surface of TiO_2 NPs is etched to form nanosheets, which subsequently scroll to form NTs.[20] More recently, an "etch and grow" process by a strong acid solution has been developed, where TiO_2 nanorods are converted into a number of small NWs, resulting in an enhanced photoelectrode surface area and increased dye loading.[21] Importantly, it has shown that the crystallinity of the new TiO_2 structures are different from the previous ones, which further increases the photoactivity.[22]

Inspired by these discoveries, herein, we have developed a postgrowth, dual "etching and doping" method of pregrown TiO_2 NW arrays in a weakly basic hydrothermal condition. A new type of crystalline core/amorphous shell TiO_2 NW is obtained with a much rougher surface, which is beneficial for the increase of the electrochemical interface area. In addition, tungsten (W) species are simultaneously incorporated into the newly grown, amorphous TiO_2 shells during this etching/regrowth process for the PEC activity increase. A high photocurrent density of 1.53 mA/cm^2 at 0.23 V *vs* Ag/AgCl (1.23 V *vs* reversible hydrogen electrode, RHE) is obtained by this W-doped core–shell TiO_2 NW photoanode, which is almost 225% of that of the pristine TiO_2 NW photoanodes. The Mott–Schottky plots and the density functional theory (DFT) simulation illustrate that the etching process decreases the band edge of TiO_2 and facilitates the charge transfer, while at the same time, the effective W-doping increases the charge carrier density inside the TiO_2 NWs. These two synergistic effects contribute to the substantially enhanced PEC performance of the W-doped core–shell TiO_2 NWs.

RESULTS AND DISCUSSION

The TiO_2 NW arrays were synthesized on FTO glass substrates by a modified hydrothermal method reported previously (Methods).[4] After the hydrothermal reaction and subsequent annealing in air, the FTO substrate is covered with a thin layer of white, uniform film. Scanning electron microscopy (SEM) images show that this film consists of dense and vertically aligned TiO_2 NW arrays (Figure 1a,b). The average NW diameter and length are 150 ± 30 nm and 2 ± 0.5 μm, respectively, and these NWs exhibit nearly rectangular cross sections (Figure 1c). The density and length of the NW arrays are well tuned by the amount of Ti precursor, acid, and reaction time, consistent with the previous reports.[4] The as-annealed TiO_2 NWs are transferred into a weak alkaline solution containing $NH_2OH \cdot HCl$, Na_2WO_4, and Na_2S (pH ~8) for a hydrothermal etching reaction to obtain the dual etched/doped TiO_2 NWs (Methods). After the reaction, no obvious color change is observed from the growth substrate (Figure S1). The average NW diameter is decreased to 100 ± 30 nm, and the NW surface becomes much rougher with granular morphologies (Figure 1d–f). The energy-dispersive X-ray spectroscopy (EDX) shows that the atomic percentages of W and Ti are 0.77% and 18.68%, respectively, corresponding to a W/Ti atomic ratio of ~4% (Figure S2). For comparison, a similar NW morphology is also obtained when Na_2WO_4 is absent from the hydrothermal reaction solution, suggesting that the combination of $NH_2OH \cdot HCl$ and Na_2S provides an etching effect for the obtained NWs (designated as the etched NWs, Figure S3a–c). On the other hand, if the hydrothermal etching solution contains Na_2WO_4 but not $NH_2OH \cdot HCl$ or Na_2S, the resulting NWs (designated as the doped NWs, Figure S3d–f) present a slightly rougher surface than the pristine TiO_2 NWs, while almost no W content (<0.1%) is detected from these NWs by EDX.

The crystal structures and the possible phase change of the dual etched/doped TiO_2 NWs are examined by X-ray diffraction (XRD), which can be well indexed into a rutile TiO_2 structure (JCPDS No. 87-0710) and the FTO substrate (Figure 2a). Compared to the pristine TiO_2 NWs, no observable shifts of all the diffraction peaks are presented after the hydrothermal treatment. No additional peaks such as tungsten oxide or sulfide are observed. Transmission electron microscopy (TEM) images exhibit that the NW surface after the hydrothermal treatment is covered with a layer of nanoparticles (Figure 2b). The sizes of nanoparticles are relatively uniform and can be tuned from sub-10 to tens of nanometers by the hydrothermal reaction time. High-resolution TEM (HRTEM) images further reveal that the NWs have a core–shell structure (Figure 2c). The NW core is single crystalline, which is clearly displayed by the corresponding fast-Fourier-transform (FFT) pattern (Figure 2c, inset). Lattice fringes of 0.322 and 0.292 nm are clearly observed, corresponding to the *d*-spacing values of the (110) and (001) planes of crystalline rutile TiO_2.[4–6] A rough, amorphous shell is observed to cover the entire NW, with an average shell thickness of ~40 nm (Figure 2d). This amorphous shell is composed of granular morphologies, with small amorphous nanoparticles of ~20 nm decorating the

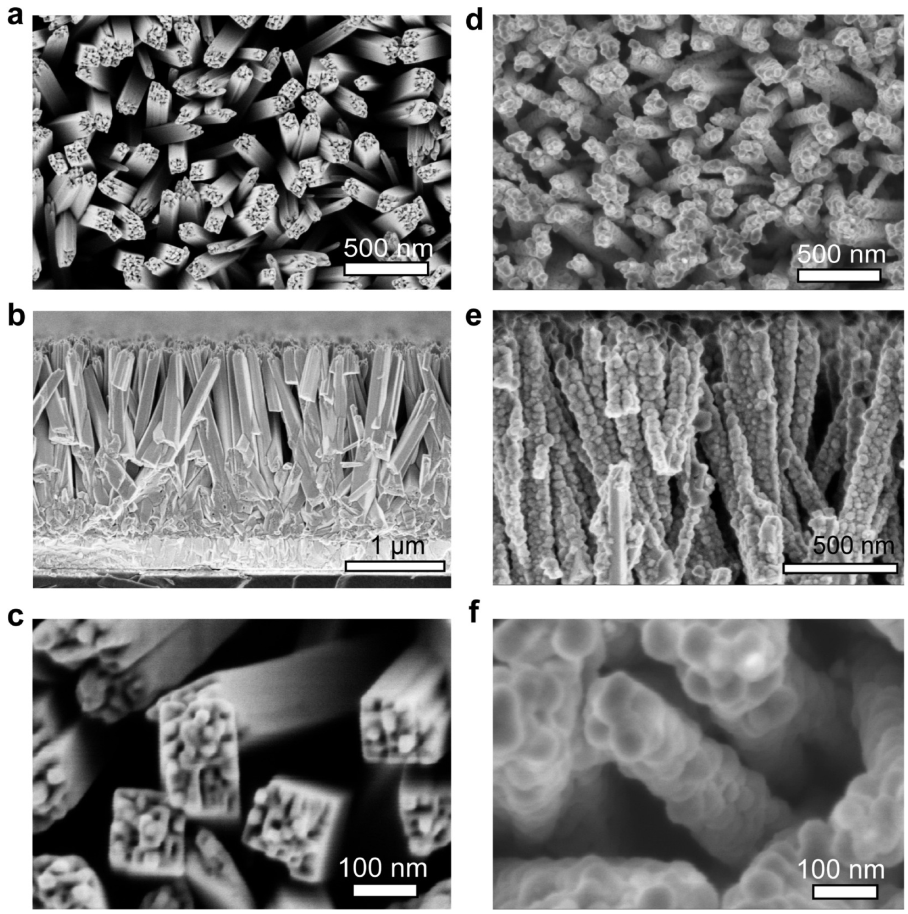

Figure 1. SEM images of (a–c) the pristine TiO_2 NWs and (d–f) the dual etched/doped TiO_2 NW arrays. (a, c, d, f) Top view. (b, e) Side view.

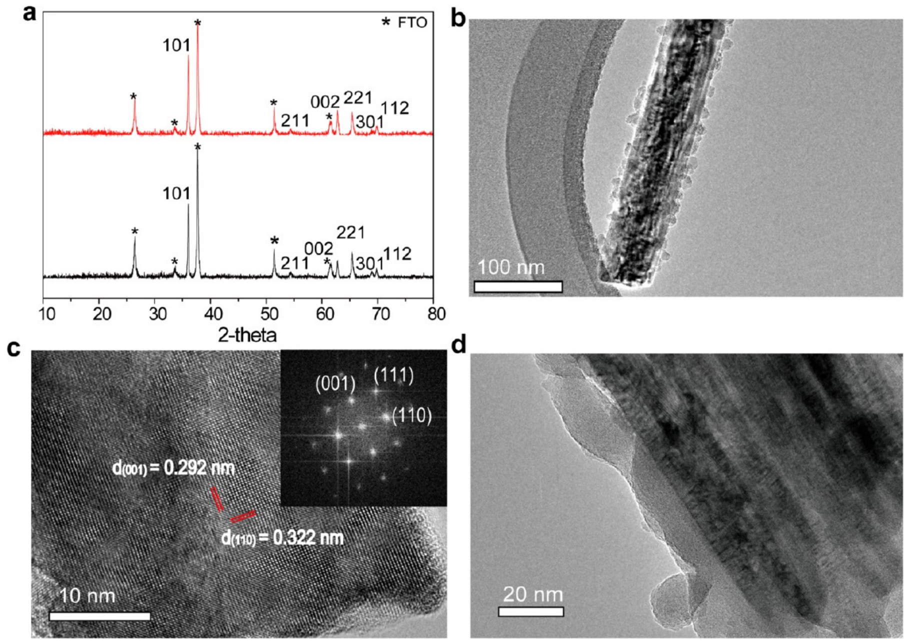

Figure 2. XRD and TEM characterization of the dual etched/doped TiO_2 NWs. (a) XRD of pristine TiO_2 NWs (lower, black curve) and dual etched/doped TiO_2 NWs (upper, red curve). The diffraction peaks of the FTO substrate are marked with asterisks. (b–d) TEM images of the NWs. Inset in c: Fast-Fourier-transform pattern of the NW.

surface. A similar NW structure is also observed for TiO_2 etched in the absence of Na_2WO_4 (*i.e.*, the etched NWs).

In addition, the successful incorporation of W dopants into the dual etched/doped TiO_2 NWs is confirmed by

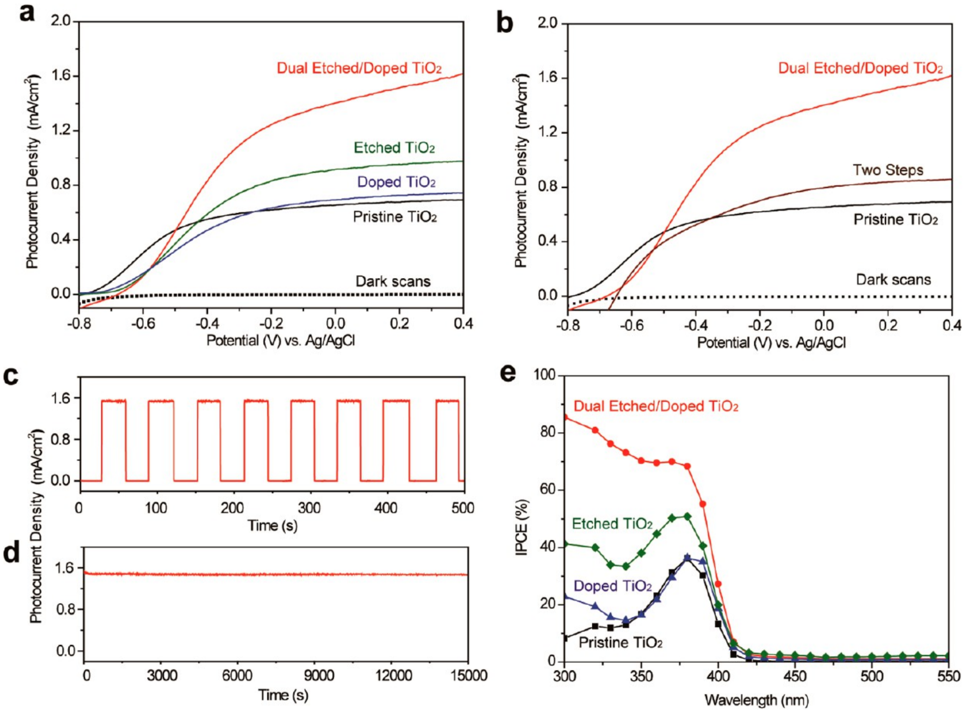

Figure 3. **(a) Photocurrent density *vs* applied potential curves of four NW photoanodes: the pristine TiO_2 NWs (black curve), the doped TiO_2 NWs (blue curve), the etched TiO_2 NWs (green curve), and the dual etched/doped TiO_2 NWs (red curve). The dark current of the dual etched/doped TiO_2 NWs is plotted as a black dotted line for comparison. (b) Photocurrent density *vs* applied potential curves of the NW photoanodes: the dual etched/doped TiO_2 NWs by one step (red curve), the two-step etching and doping TiO_2 NWs (brown curve), and the pristine TiO_2 NWs (black curve). (c, d) Photocurrent density *vs* time of the dual etched/doped TiO_2 NWs measured at 0.23 V *vs* Ag/AgCl (c) at repeated on/off cycles of simulated sunlight illumination and (d) under continuous simulated sunlight illumination. (e) IPCE spectra of the four NW samples measured at −0.2 V *vs* Ag/AgCl.**

X-ray photoelectron spectroscopy (XPS) (Figure S4). The peaks centered at 458.6, 464.4, and 532.8 eV are attributed to Ti $2p_{3/2}$, Ti $2p_{1/2}$, and O 1s, respectively. The peak from 32 to 38 eV is deconvoluted into three peaks. The peaks located at 34.9 and 37.4 eV are assigned to $4f_{7/2}$ and $4f_{5/2}$ of the W(VI), whereas the peak at 36.5 eV is attributed to the Ti 3p level.[13] Taken together, these results indicate that the obtained dual etched/doped NWs are W-doped, core−shell TiO_2 NWs, in which the core and the shell are crystalline (c-TiO_2) and amorphous TiO_2 (a-TiO_2), respectively, and W (mainly existing as W^{6+}) is doped in the NWs through the one-step etching−doping process. Neither EDX nor XPS detects the existence of S, suggesting almost no sulfide or S-doping is formed under our experimental conditions.

To evaluate the PEC conversion activity of the dual etched/doped TiO_2 NWs, these NWs are fabricated as photoanodes with an exposed surface area of ~1 cm². A platinum wire and an Ag/AgCl electrode are used as the counter and reference electrodes, respectively, and the PEC measurement is carried out in a 1 M KOH solution (Methods). The reversible hydrogen electrode potential can be converted from the Ag/AgCl reference potential as RHE = $V_{\text{vs Ag/AgCl}} + E°_{\text{Ag/AgCl}} + 0.059 \times \text{pH} = V_{\text{vs Ag/AgCl}} + 1.0$ V,[4] where $E°_{\text{Ag/AgCl}}$ is 0.1976 V at 25 °C. For comparison, photoanodes made of the pristine TiO_2 NWs, the doped NWs, and the etched NWs are also measured under similar conditions. Under air mass (AM) 1.5G simulated solar light illumination, the photocurrent density of the pristine TiO_2 NWs is 0.68 mA/cm² at 0.23 V *vs* Ag/AgCl (1.23 V *vs* RHE) (Figure 3a, black curve), comparable to previously reported values.[4−6] A similar photocurrent density is recorded from the doped NWs (Figure 3a, blue curve), which is 0.73 mA/cm² at 0.23 V *vs* Ag/AgCl, suggesting an insignificant effect from the postgrowth W-doping approach, which is also in good accord with the negligible W content from the EDX result. On the other hand, a clear increase of the photocurrent is observed from the etched NWs, which is 0.96 mA/cm² at 0.23 V *vs* Ag/AgCl (Figure 3a, green curve), indicating the etching effect on the photoactivity of TiO_2 NWs. Remarkably, the dual etched/doped TiO_2 NWs exhibit the highest photocurrent density among these four photoanodes (Figure 3a, red curve), which reaches 1.53 mA/cm² at 0.23 V *vs* Ag/AgCl and is 225% of the pristine TiO_2 NWs.

This simultaneous, dual etching and doping effect on the PEC activity of the TiO_2 NWs is further compared with TiO_2 NWs that are sequentially etched, followed by the W-doping process (Figure 3b). Interestingly, the magnitude of photocurrent density increase by this sequential, two-step etching/doping process is similar to that of the etched NW (*i.e.*, made by etching only),

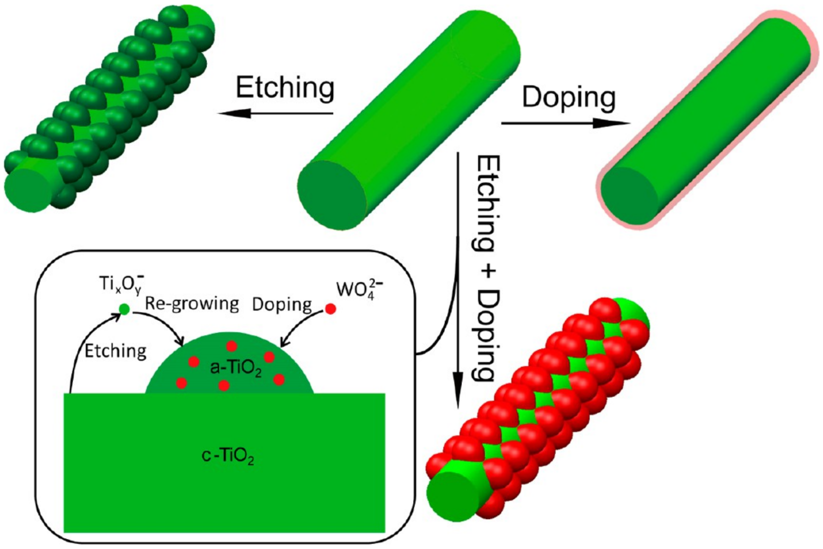

Figure 4. Schematic illustration of the simultaneous etching and W-doping mechanism for TiO_2 NWs.

but much less than that of the one-step dual etching/doping approach. These photocurrent measurements clearly indicate that the simultaneous etching and doping effects contribute substantially to the increase of the W-doping content inside TiO_2 NWs and the corresponding photocurrent density, while the post-doping-only method is much less effective under this reaction temperature. Moreover, the time-dependent photocurrent measurement of the dual etched/doped TiO_2 NWs shows a stable photocurrent density of ~1.53 mA/cm^2 at 0.23 V *vs* Ag/AgCl, as well as an excellent correlation with the on/off cycles of simulated solar light (Figure 3c). This photocurrent is highly stable under continuous solar illumination for 15 000 s without observable degradation (Figure 3d), indicating excellent chemical and structural stability of the dual etched/doped TiO_2 NWs for long-term PEC conversion.

To further evaluate the external quantum efficiency of these four NW samples at different wavelength regions, the incident photo-to-current conversion efficiency (IPCE) is measured at −0.2 V *vs* Ag/AgCl from 300 to 550 nm (Figure 3e), which reveals several features. First, the photocurrent responses of all four NW samples are mainly located in the wavelength region of 300−420 nm and decrease to almost zero for wavelengths above 420 nm. This result is consistent with the band gap of rutile TiO_2 (~3.0 eV)[5] and also indicates that either the etching or W-doping presented in our work does not modulate the band gap of TiO_2 in an observable magnitude, which is consistent with the UV−vis reflectance spectra collected over these samples (Figure S5) as well as the literature.[6] Second, the "doped" TiO_2 NWs (blue curve) show a similar IPCE profile to that of the pristine TiO_2 NWs (black curve), indicating W dopants are not incorporated into the TiO_2 NWs efficiently by the postgrowth-only hydrothermal treatment at temperatures lower than 200 °C. This phenomenon is distinct from a recent report, where W atoms are doped into TiO_2 NWs by a high-temperature (1100 °C) sol-flame doping method.[6] Third, compared to the IPCE value between 10% and 30% for the pristine TiO_2 NWs, the etched TiO_2 NWs (green curve) are increased to 30−50%, indicating a higher efficiency in the conversion of UV light. This phenomenon may be attributed to the increase of surface area of the etched TiO_2 NWs, which provides more electrochemical reaction locations at the TiO_2/electrolyte interface. In addition, the amorphous TiO_2 shell may also present a greater photocatalytic activity than the crystalline phase, as suggested by reports for CoO_x and NiO_x recently.[22,23] Fourth, the dual etched/doped TiO_2 NWs (red curve) present the highest IPCE profile, which is over 70−90% in the UV range 300−400 nm. Compared to the UV−vis reflectance spectra of the dual etched/doped TiO_2 NWs and the pristine ones (Figure S5), these results suggest that the PEC conversion improvement is not mainly attributed to the light absorption enhancement in either the UV or visible region, but some other factors that are resulting from the combination effect of the etching and W-doping.

On the basis of the characterization above of the four types of TiO_2 NWs, a simultaneous etching/regrowth and doping mechanism is proposed for the dual etched/doped TiO_2 NWs (Figure 4). First, it has been reported that crystalline TiO_2 can be etched in basic, hydrothermal conditions. During this process, the amorphous TiO_2 phase, with similar or substantially different morphologies, can regrow over the initial crystalline surface or in the solution, such as forming TiO_2 nanotubes from the etched TiO_2 nanoparticles.[18,19] Recent studies have also shown that a sodium titanate phase is formed over the TiO_2 nanoparticles first, followed by turning into amorphous TiO_2 in alkaline conditions.[22,24] In our weakly alkaline etching solution with pH ≈ 8,

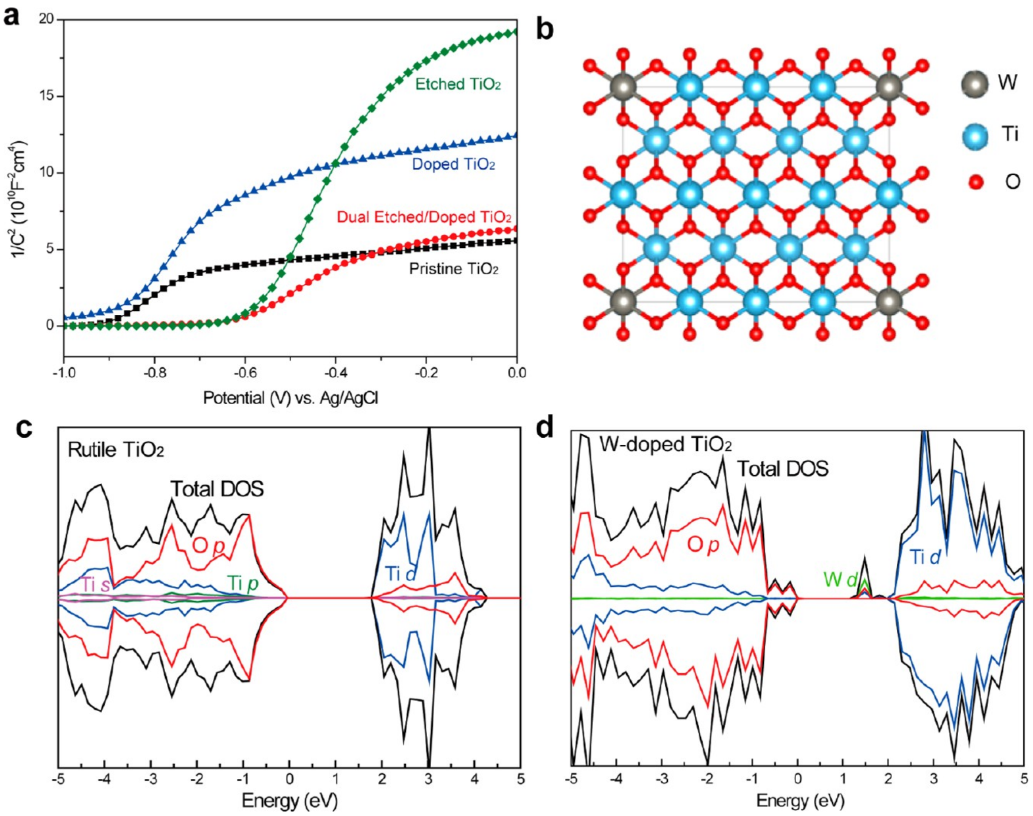

Figure 5. (a) Mott−Schottky plots of the four NW samples. (b) Supercell model for the W-doped rutile TiO_2. The gray, blue, and red spheres represent W, Ti, and O atoms, respectively. (c, d) DOS and PDOS for (c) the pristine TiO_2 NWs and (d) W-doped TiO_2 NWs.

TiO_2 NWs are first etched to sodium titanate and subsequently converted to amorphous TiO_2 nanoparticles. On the other hand, when Na_2WO_4 is added into the weakly alkaline solution, W^{6+} ions can be incorporated into the amorphous TiO_2 shell that is formed from the etching/regrowth process, leading to both an increase of surface area and effective W-doping inside the TiO_2 NWs.

The mechanism of the photocurrent enhancement for the dual etched/doped TiO_2 NWs is interrogated by electrochemical impedance spectroscopy (EIS) measurements, which can provide a semiquantitative comparison of different samples with similar material composition, morphology, and device geometry.[25] The Mott−Schottky plots of the pristine, the etched, the doped, and the dual etched/doped TiO_2 NWs are displayed in Figure 5a. All four samples show positive slopes in the corresponding Mott−Schottky plots, as expected for n-type TiO_2 semiconductors.[26] According to the Mott−Schottky equation,[27]

$$\frac{1}{C^2} = \frac{2}{N_d e \varepsilon_0 \varepsilon}\left(E - E_{FB} - \frac{kT}{e}\right)$$

where C is the space charge capacitance in the semiconductor, N_d is the charge carrier density, e is the elemental charge, ε_0 and ε are the vacuum permittivity and the relative permittivity of the semiconductor, respectively, E is the applied potential, E_{FB} is the flat band potential, T is the temperature, and k is the Boltzmann constant. The flat band potential (E_{FB}) value is estimated by extrapolating the Mott−Schottky plots to the x-axis (*i.e.*, $1/C^2 = 0$) to get the intercept. The charge carrier density (N_d) can be calculated from the Mott−Schottky plots using the following equation:[27]

$$N_d = \frac{2}{e\varepsilon_0\varepsilon}\left(\frac{dE}{d\left(\frac{1}{C^2}\right)}\right)$$

For TiO_2 ($\varepsilon = 170$),[5] the E_{FB} and N_d values are calculated and summarized in Table 1.

Compared to the pristine TiO_2 NWs, both the etched TiO_2 NWs and the dual etched/doped TiO_2 NWs show positive shifts of E_{FB}, suggesting a decrease in the bending of band edges.[27] The flat band shift has a major effect on the increase of the photocurrent for the etched and the dual etched/doped NW samples. This decrease of band edge bending can be attributed to the increased TiO_2/electrolyte interface for PEC reaction that can facilitate the charge carrier transfer efficiency,[28,29] which is also similar to a previous report of Pd quantum dots-sensitized TiO_2 nanotubes.[27] In addition, both the etched TiO_2 and the doped TiO_2 NWs show a decrease of charge carrier density compared to that of the pristine TiO_2. For the doped TiO_2 NWs, the

TABLE 1. Flat Band Potential (E_{FB}) and the Charge Carrier Density (N_d) of TiO_2 NWs

sample	E_{FB} (V) *vs* Ag/AgCl	$N_d/10^{18}$ cm^{-3}
pristine TiO_2 NW	−0.89	3.86
doped TiO_2 NW	−0.87	2.06
etched TiO_2 NW	−0.58	1.36
dual etched/doped TiO_2 NW	−0.60	5.04

distribution of W atoms is not inside the NWs, but on the surface of NWs. This high dopant concentration on the surface, or the surface roughness created by etching, increases the number of recombination centers for charge carriers, resulting in lower carrier density.[29,30] For the dual etched/doped TiO_2 NWs, the dopants are more uniformly distributed over the NW shell due to the etching/regrowth process, thus leading to an increase of charge carrier density. Notably, the dual etched/doped NWs show an increase of N_d, as a much more uniform W-doping along the etching/regrowth process can substantially increase the charge carrier density inside TiO_2 NWs.[6]

Finally, the DFT calculation is carried out to illustrate the effect of W-doping on TiO_2 (Methods) and to support the above explanation. The doped system is constructed from a relaxed (2 × 2 × 4) 96-atom rutile supercell, and a W atom is substituted for a Ti atom (Figure 5b). To investigate the W-doping-induced changes in the electronic structure of rutile TiO_2, the total density of states (DOS) and the projected density of states (PDOS) for pristine rutile TiO_2 (Figure 5c) and the W-doped TiO_2 96-atom supercell (Figure 5d) are plotted. The optimized lattice parameters for pure rutile TiO_2 are found to be $a = 4.65$ Å and $c = 2.97$ Å, in good agreement with experimental and other theoretical results,[31,32] indicating that our DFT model is reasonable, although the calculated band-gap energy for pure rutile TiO_2 (1.80 eV) is lower than the experimental value of ~3.0 eV, as the band-gap energy is underestimated by the Perdew–Burke–Ernzerhof method, similar to previous reports.[32] However, the discussion about the band gap is not affected by this underestimation, as only changes between band gaps are compared. For the pristine rutile TiO_2, the valence band edge is mostly composed of O 2p states, and the conduction band edge mainly consists of Ti 3d states, in agreement with the previous study.[33] For the W-doped system, there is little shift of the position in the valence and conduction band edges, resulting in no band-gap narrowing, which is consistent with our IPCE result (Figure 3e) and reflectance spectrum (Figure S5). W 5d states are localized in the band gap. The gap states are close to the conduction band edge, so the charge carriers on the gap states can be easily excited into the conduction band, thus increasing the charge carrier density. The gap states are also far from the valence band edge, so it is difficult for the holes on the valence band to be excited to the gap states and form recombination centers.[32] This process increases the possibility of exciting electrons, and subsequently increases the charge carrier density, in good accord with the Mott–Schottky plots (Figure 5a). Taken together, our results show that both the increase of the charge carrier density and the charge transfer efficiency lead to the enhanced PEC conversion activity for the dual etched/doped TiO_2 NWs.

CONCLUSIONS

In summary, we have developed a new hydrothermal, simultaneous etching and doping method that allows for converting the pregrown rutile TiO_2 NWs into W-doped core–shell TiO_2 NWs. The amorphous TiO_2 shell with a rough surface results from the etching/regrowth mechanism, while effective W-doping into the amorphous shell is simultaneously achieved, which offers a synergistic effect on the PEC performance. A much enhanced photoconversion activity has been measured by the W-doped TiO_2 core–shell NWs compared to the pristine TiO_2 NWs under similar conditions, which is attributed to the increase of charge carrier density and charge transport kinetics. In addition, this simultaneous etching and growth process is convenient and low cost and takes place at relatively low hydrothermal temperature and in almost neutral conditions, which may offer a general means for incorporation of a variety of dopants into TiO_2. Combined with the DFT calculation, our studies can further inspire exploration of the postgrowth doping of other transition metal oxide photoelectrodes with enhanced PEC conversion activity.

METHODS

Synthesis of Rutile TiO_2 Nanowires. The pristine TiO_2 nanowires were synthesized on FTO glass substrates using a modified hydrothermal method report elsewhere.[4] In a typical experiment, 13 mL of concentrated hydrochloric acid (37 wt %) was diluted by 15 mL of deionized (DI) water, and then 300 μL of tetrabutyl titanate was added in the solution. After 15 min of constant stirring, the solution mixture and a clean FTO glass substrate were transferred into a 50 mL sealed Teflon reactor, which was then kept in an oven at 150 °C for 12 h. After that, the FTO substrate was rinsed with DI water and dried by compressed N_2. Finally, the sample was annealed in air at 450 °C for 2 h.

Simultaneous Etching and W-Doping of TiO_2 NWs. The as-prepared TiO_2 NWs on a FTO substrate were placed in a 50 mL sealed Telfon reactor, containing 0.725 g of hydroxylamine hydrochloride ($NH_2OH \cdot HCl$), 1.20 g of sodium sulfide nonahydrate ($Na_2S \cdot 9H_2O$), 1.852 g of sodium tungstate dehydrate (Na_2WO_4), and 30 mL of DI water. The reactor was kept at 180 °C for 10 h. After that, the sample was thoroughly washed with DI water and dried by compressed N_2. For the etching-only experiments, the reaction solution contained only $NH_2OH \cdot HCl$, Na_2S, and DI water. For the doping-only experiments, the reaction solution contained only Na_2WO_4 and DI water. All other experimental conditions remained the same.

Photoelectrochemical Measurement. Photocurrent was measured in a three-electrode system, with the TiO_2 NW photoanode as the working electrode, a coiled Pt wire as the counter electrode, and a Ag/AgCl as the reference electrode. Linear sweep voltammetry was carried out with a CHI660D potentiostat (CH Instruments Co.) *vs* Ag/AgCl in 1 M KOH (pH = 13.6). The photoanode was illuminated with 100 mW/cm^2 simulated sunlight (Newport Co., USA). Mott−Schottky plots were measured at a frequency of 5 kHz in the dark.

Density Functional Theory Calculation. The DFT method is used to provide the electronic structure of a doped system. The spin-polarized DFT calculation is supported by the Vienna *ab initio* simulation package (VASP).[34] The interaction between the core electrons and the valence electrons is described by the projector augmented wave (PAW) approach.[35] A Hubbard-like, localized term is added to the Perdew−Burke−Ernzerhof generalized gradient approximation (GGA) exchange correlation functional,[36] which is called GGA+U and widely applied for systems with localized d and f electrons.[37] The value of U is set to be 6.2 eV.[38] The convergence threshold for self-consistent energy error is 0.0006 eV. The doped system is constructed from a relaxed (2 × 2 × 4) 96-atom rutile supercell. A W atom is substituted for a Ti atom. Testing the plane wave energy cutoff and k-point sampling gives a 520 eV plane wave energy cutoff and a (3 × 3 × 3) k-point sampling mesh.

Conflict of Interest: The authors declare no competing financial interest.

Acknowledgment. G.Z. thanks the following funding agencies for supporting this work: the National Key Basic Research Program of China (2013CB934104), the NSF of China (21322311, 21071033), the Program for New Century Excellent Talents in University (NCET-10-0357), the Shanghai Pujiang Program (10PJ1401000), and the Program for Professor of Special Appointment (Eastern Scholar) at Shanghai Institutions of Higher Learning. X.G. is partially supported by the National Key Basic Research Program of China (2012CB921400) and the NSF of China. J.T. acknowledges the Interdisciplinary Outstanding Doctoral Research Funding of Fudan University.

Supporting Information Available: Optical images, EDX spectroscopy, SEM images, XPS, and UV−vis absorption characterization of the samples. This material is available free of charge *via* the Internet at http://pubs.acs.org.

REFERENCES AND NOTES

1. Hochbaum, A. I.; Yang, P. Semiconductor Nanowires for Energy Conversion. *Chem. Rev.* **2010**, *110*, 527–546.
2. Walter, M. G.; Warren, E. L.; McKone, J. R.; Boettcher, S. W.; Mi, Q.; Santori, E. A.; Lewis, N. S. Solar Water Splitting Cells. *Chem. Rev.* **2010**, *110*, 6446–6473.
3. Wang, Y.; Wang, T.; Da, P.; Xu, M.; Wu, H.; Zheng, G. Silicon Nanowires for Biosensing, Energy Storage, and Conversion. *Adv. Mater.* **2013**, 10.1002/adma.201301943.
4. Xu, M.; Da, P.; Wu, H.; Zhao, D.; Zheng, G. Controlled Sn-Doping in TiO_2 Nanowire Photoanodes with Enhanced Photoelectrochemical Conversion. *Nano Lett.* **2012**, *12*, 1503–1508.
5. Wang, G.; Wang, H.; Ling, Y.; Tang, Y.; Yang, X.; Fitzmorris, R. C.; Wang, C.; Zhang, J. Z.; Li, Y. Hydrogen-Treated TiO_2 Nanowire Arrays for Photoelectrochemical Water Splitting. *Nano Lett.* **2011**, *11*, 3026–3033.
6. Cho, I. S.; Lee, C. H.; Feng, Y.; Logar, M.; Rao, P. M.; Cai, L.; Kim, D. R.; Sinclair, R.; Zheng, X. Codoping Titanium Dioxide Nanowires with Tungsten and Carbon for Enhanced Photoelectrochemical Performance. *Nat. Commun.* **2013**, *4*, 1723.
7. Xia, X.; Luo, J.; Zeng, Z.; Guan, C.; Zhang, Y.; Tu, J.; Zhang, H.; Fan, H. J. Integrated Photoelectrochemical Energy Storage: Solar Hydrogen Generation and Supercapacitor. *Sci. Rep.* **2012**, *2*, 981.
8. Wang, H.; Song, Y.; Liu, W.; Yao, S.; Zhang, W. Template Synthesis and Characterization of TiO_2 Nanotube Arrays by the Electrodeposition Method. *Mater. Lett.* **2013**, *93*, 319–321.
9. Zhang, Z.; Zhang, L.; Hedhili, M. N.; Zhang, H.; Wang, P. Plasmonic Gold Nanocrystals Coupled with Photonic Crystal Seamlessly on TiO_2 Nanotube Photoelectrodes for Efficient Visible Light Photoelectrochemical Water Splitting. *Nano Lett.* **2012**, *13*, 14–20.
10. Miao, Z.; Xu, D.; Ouyang, J.; Guo, G.; Zhao, X.; Tang, Y. Electrochemically Induced Sol-Gel Preparation of Single-Crystalline TiO_2 Nanowires. *Nano Lett.* **2002**, *2*, 717–720.
11. Feng, X.; Zhu, K.; Frank, A. J.; Grimes, C. A.; Mallouk, T. E. Rapid Charge Transport in Dye-Sensitized Solar Cells Made from Vertically Aligned Single-Crystal Rutile TiO_2 Nanowires. *Angew. Chem., Int. Ed.* **2012**, *124*, 2781–2784.
12. Mi, Q.; Zhanaidarova, A.; Brunschwig, B. S.; Gray, H. B.; Lewis, N. S. A Quantitative Assessment of the Competition Between Water and Anion Oxidation at WO_3 Photoanodes in Acidic Aqueous Electrolytes. *Energy Environ. Sci.* **2012**, *5*, 5694–5700.
13. Zhang, X.; Liu, F.; Huang, Q.-L.; Zhou, G.; Wang, Z.-S. Dye-Sensitized W-Doped TiO_2 Solar Cells with a Tunable Conduction Band and Suppressed Charge Recombination. *J. Phys. Chem. C* **2011**, *115*, 12665–12671.
14. Feng, D.; Luo, W.; Zhang, J.; Xu, M.; Zhang, R.; Wu, H.; Lv, Y.; Asiri, A. M.; Khan, S. B.; Rahman, M. M.; *et al.* Multi-Layered Mesoporous TiO_2 Thin Tilms with Large Pores and Highly Crystalline Frameworks for Efficient Photoelectrochemical Conversion. *J. Mater. Chem. A* **2013**, *1*, 1591–1599.
15. Liang, F.; Zhang, J.; Zheng, L.; Tsang, C.-K.; Li, H.; Shu, S.; Cheng, H.; Li, Y. Y. Selective Electrodeposition of Ni into the Intertubular Voids of Anodic TiO_2 Nanotubes for Improved Photocatalytic Properties. *J. Mater. Res.* **2013**, *28*, 405–410.
16. Obata, K.; Irie, H.; Hashimoto, K. Enhanced Photocatalytic Activities of Ta, N Co-Doped TiO_2 Thin Films under Visible Light. *Chem. Phys.* **2007**, *339*, 124–132.
17. Franking, R.; Li, L.; Lukowski, M. A.; Meng, F.; Tan, Y.; Hamers, R. J.; Jin, S. Facile Post-Growth Doping of Nanostructured Hematite Photoanodes for Enhanced Photoelectrochemical Water Oxidation. *Energy Environ. Sci* **2013**, *6*, 500–512.
18. Kasuga, T.; Hiramatsu, M.; Hoson, A.; Sekino, T.; Niihara, K. Formation of Titanium Oxide Nanotube. *Langmuir* **1998**, *14*, 3160–3163.
19. Du, G.; Chen, Q.; Che, R.; Yuan, Z.; Peng, L.-M. Preparation and Structure Analysis of Titanium Oxide Nanotubes. *Appl. Phys. Lett.* **2001**, *79*, 3702.
20. Nakahira, A.; Kubo, T.; Numako, C. Formation Mechanism of TiO_2-Derived Titanate Nanotubes Prepared by the Hydrothermal Process. *Inorg. Chem.* **2010**, *49*, 5845–5852.
21. Guo, W.; Xu, C.; Wang, X.; Wang, S.; Pan, C.; Lin, C.; Wang, Z. L. Rectangular Bunched Rutile TiO_2 Nanorod Arrays Grown on Carbon Fiber for Dye-Sensitized Solar Cells. *J. Am. Chem. Soc.* **2012**, *134*, 4437–4441.
22. Smith, R. D.; Prévot, M. S.; Fagan, R. D.; Zhang, Z.; Sedach, P. A.; Siu, M. K. J.; Trudel, S.; Berlinguette, C. P. Photochemical Route for Accessing Amorphous Metal Oxide Materials for Water Oxidation Catalysis. *Science* **2013**, *340*, 60–63.
23. Kanan, M. W.; Nocera, D. G. *In Situ* Formation of an Oxygen-Evolving Catalyst in Neutral Water Containing Phosphate and Co^{2+}. *Science* **2008**, *321*, 1072–1075.
24. Kiatkittipong, K.; Ye, C.; Scott, J.; Amal, R. Understanding Hydrothermal Titanate Nanoribbon Formation. *Cryst. Growth Des.* **2010**, *10*, 3618–3625.
25. Lin, Y.; Zhou, S.; Sheehan, S. W.; Wang, D. Nanonet-Based Hematite Heteronanostructures for Efficient Solar Water Splitting. *J. Am. Chem. Soc.* **2011**, *133*, 2398–2401.
26. Khan, S. U.; Al-Shahry, M.; Ingler, W. B. Efficient Photochemical Water Splitting by a Chemically Modified n-TiO_2. *Science* **2002**, *297*, 2243–2245.
27. Ye, M.; Gong, J.; Lai, Y.; Lin, C.; Lin, Z. High-Efficiency Photoelectrocatalytic Hydrogen Generation Enabled by Palladium Quantum Dots-Sensitized TiO_2 Nanotube Arrays. *J. Am. Chem. Soc.* **2012**, *134*, 15720–15723.
28. Liao, J.-Y.; Lei, B.-X.; Chen, H.-Y.; Kuang, D.-B.; Su, C.-Y. Oriented Hierarchical Single Crystalline Anatase TiO_2 Nanowire Arrays on Ti-Foil Substrate for Efficient Flexible Dye-Sensitized Solar Cells. *Energy Environ. Sci.* **2012**, *5*, 5750–5757.

29. Lv, M.; Zheng, D.; Ye, M.; Xiao, J.; Guo, W.; Lai, Y.; Sun, L.; Lin, C.; Zuo, J. Optimized Porous Rutile TiO_2 Nanorod Arrays for Enhancing the Efficiency of Dye-Sensitized Solar Cells. *Energy Environ. Sci.* **2013**, *6*, 1615–1622.
30. Choi, W.; Termin, A.; Hoffmann, M. R. The Role of Metal Ion Dopants in Quantum-Sized TiO_2: Correlation between Photoreactivity and Charge Carrier Recombination Dynamics. *J. Phys. Chem.* **1994**, *98*, 13669–13679.
31. Burdett, J. K.; Hughbanks, T.; Miller, G. J.; Richardson, J. W.; Smith, J. V. Structural-Electronic Relationships in Inorganic Solids: Powder Neutron Diffraction Studies of the Rutile and Anatase Polymorphs of Titanium Dioxide at 15 and 295 K. *J. Am. Chem. Soc.* **1987**, *109*, 3639–3646.
32. Yang, K.; Dai, Y.; Huang, B.; Han, S. Theoretical Study of N-Doped TiO_2 Rutile Crystals. *J. Phys. Chem. B* **2006**, *110*, 24011–24014.
33. Woicik, J. C.; Nelson, E. J.; Kronik, L.; Jain, M.; Chelikowsky, J. R.; Heskett, D.; Berman, L. E.; Herman, G. S. Hybridization and Bond-Orbital Components in Site-Specific X-Ray Photoelectron Spectra of Rutile TiO_2. *Phys. Rev. Lett.* **2002**, *89*, 077401.
34. Kresse, G.; Hafner, J. *Ab Initio* Molecular-Dynamics Simulation of the Liquid-Metal-Amorphous-Semiconductor Transition in Germanium. *Phys. Rev. B* **1994**, *49*, 14251–14269.
35. Blöchl, P. E. Projector Augmented-Wave Method. *Phys. Rev. B* **1994**, *50*, 17953–17979.
36. Perdew, J. P.; Burke, K.; Ernzerhof, M. Generalized Gradient Approximation Made Simple. *Phys. Rev. Lett.* **1996**, *77*, 3865–3868.
37. Anisimov, V. I.; Zaanen, J.; Andersen, O. K. Band Theory and Mott Insulators: Hubbard U Instead of Stoner I. *Phys. Rev. B* **1991**, *44*, 943–954.
38. Jain, A.; Ong, S. P.; Hautier, G.; Chen, W.; Richards, W. D.; Dacek, S.; Cholia, S.; Gunter, D.; Skinner, D.; Ceder, G.; *et al.* Commentary: The Materials Project: A Materials Genome Approach to Accelerating Materials Innovation. *APL Mater.* **2013**, *1*, 011002.